Single image Fourier ring correlation

Rieger, Bernd; Droste, Isabel; Gerritsma, Fabian; Brink, Tip Ten; Stallinga, Sjoerd

DOI
10.1364/OE.524683

Publication date
2024

Document Version
Final published version

Published in
Optics Express

Research Article Vol. 32, No. 12 / 3 Jun 2024 / Optics Express 21767
Optics EXPRESS

Single image Fourier ring correlation

BERND RIEGER,[1,2] ISABEL DROSTE,[1] FABIAN GERRITSMA,[1] TIP TEN BRINK,[1] AND SJOERD STALLINGA[1,3]

[1]Department of Imaging Physics, Delft University of Technology, Delft, The Netherlands
[2]b.rieger@tudelft.nl
[3]s.stallinga@tudelft.nl

Abstract: We address resolution assessment for (light super-resolution) microscopy imaging. In modalities where imaging is not diffraction limited, correlation between two noise independent images is the standard way to infer the resolution. Here we take away the need for two noise independent images by computationally splitting one image acquisition into two noise independent realizations. This procedure generates two Poisson noise distributed images if the input is Poissonian distributed. As most modern cameras are shot-noise limited this procedure is directly applicable. However, also in the presence of readout noise we can compute the resolution faithfully via a correction factor. We evaluate our method on simulations and experimental data of widefield microscopy, STED microscopy, rescan confocal microscopy, image scanning microscopy, conventional confocal microscopy, and transmission electron microscopy. In all situations we find that using one image instead of two results in the same computed image resolution.

1. Introduction

Abbe's diffraction limit, restricting the resolution of an imaging system to lengths scales on the order of λ/NA, with λ the wavelength and NA the Numerical Aperture of the imaging system, has been the cornerstone of optical imaging systems for over a century. The advent of super-resolution microscopy has resulted in numerous ways to circumvent the diffraction limit [1–4]. This has raised the question how the resolution should be assessed if the diffraction limit is no longer appropriate. Several years ago we have proposed the concept of Fourier Ring Correlation (FRC) for optical imaging and in particular for single molecule localization microscopy (SMLM) [5], which checks the internal consistency of the image across all length scales. Initially Fourier Ring or Shell Correlation was introduced for electron microscopy (EM) [6,7] to assess resolution because the imaging system is not diffraction limited but signal-to-noise limited. The correlation approach needs two noise independent image of the same object, and is computed from the correlation between these two images, averaged over rings or shells in Fourier space. This correlation is high at a certain spatial frequency when signal dominates and low when noise dominates. The image resolution is defined as the length scale where the correlation level drops below a suitably defined threshold value. This threshold is usually taken to be 1/7. This value has been derived accounting for the 50% Signal-to-Noise-Ratio (SNR) in the two images [8]. This approach works well with SMLM, as then there is a natural way to generate two independent images, i.e. splitting the time series dataset by simply grouping the total set of localization events in two sub-groups. Also in transmission electron microscopy (TEM) images this approach works well as modern cameras acquire many frames at high frame rate and the actual image is an average of this.

The FRC has also been applied to conventional widefield fluorescence microscopy by us [5], and to STimulated Emission Depletion (STED) in Ref. [9], but has the obvious drawback for

#524683 https://doi.org/10.1364/OE.524683
Journal © 2024 Received 25 Mar 2024; revised 20 May 2024; accepted 21 May 2024; published 30 May 2024

Optics EXPRESS

those modalities that two images must be taken. This drawback pertains to other modalities such as Structured Illumination Microscopy (SIM) [10] as well. This is inconvenient from a practical point of view. Recently, a checkerboard type of image splitting approach has been proposed for evaluating the FRC from a "single" image [11]. In this approach each pixel of the image is assigned to one of two images based on a checkerboard-like geometry. The drawback of this method is that it requires large oversampling (pixel density twice above the Nyquist limit), or at least a sufficiently low SNR at small length scales such that the derived FRC resolution is well above the sampling distance. In fact, this method does not deal with two identical images that only deviate in noise, but only approximately due to the pixel assignment.

A different method to evaluate the resolution from a single image is the decorrelation analysis of Ref. [22]. They perform a phase autocorrelation for a series of filtered images and from this determine the highest spatial frequency present at a sufficient SNR. For this analysis to be reliable the visualization of the image data is important and affects the outcome in cases where no natural visualisation is present in terms of pixels as with SMLM. In addition, the decorrelation analysis is not available for 3D images, nor can it assess if the resolution is isotropic.

Here, we propose a single image splitting procedure that overcomes the drawbacks of the checkerboard method and enables the use of FRC on one image. Our procedure makes use of a single image acquisition, works for any sampling density, and is straightforward to apply. The main idea is to create two noise independent images from one image by randomly splitting each pixel value into two smaller values according to the binomial distribution. In this manner the Poisson distribution of the input image data is maintained in the two image halves. The method relies on the fact that modern day sCMOS or EMCCD cameras are shot noise limited.

The contents of this paper are as follows. In section 2 we introduce the random binomial data splitting method, and in section 3 we evaluate its performance on simulation data. In section 4 we test the method on widefield microscopy data, on data acquired with STED microscopy, and use it to compare Rescan Confocal Microscopy (RCM) [12] to Image Scanning Microscopy (ISM) [13] and conventional confocal scanning microscopy. We also demonstrate the validity of the method for Transmission Electron Microscopy (TEM) data. The paper is concluded in section 5 with a summary of the conclusions and with an outlook on other applications of the random binomial data splitting method.

2. Theory

2.1. Random binomial data splitting

In the limit in which shot noise dominates over other noise sources such as readout noise, we can split an image into two noise independent halves. The noise in the two halves follows Poisson statistics, just like the noise in the original image. This approach was suggested by York [14], our proof below is based on Fried [15], and the important steps are reproduced here.

Consider first a single Poisson random variable n with rate μ, e.g. the photon count of a single pixel of an image. The observed photon count n is split in two parts $n = n_1 + n_2$ according to binomial statistics with success probability p. We will use $p = 0.5$ later, but the value of p is irrelevant for the proof. Note that this splitting allows to create "true" observations with lower photon count than an actual image by adjusting the success probability p. This procedure might be of interest for learning based approaches as you can generate suitable training images in silicio.

Starting with the Poisson probability distribution:

$$P_{\text{Poisson}}(n|\mu) = \frac{e^{-\mu}\mu^n}{n!}, \tag{1}$$

and the binomial distribution with success probability p:

$$P_{\text{binomial}}(n_1, n_2|n_1 + n_2, p) = \frac{(n_1 + n_2)!}{n_1!n_2!} p^{n_1} (1-p)^{n_2}, \tag{2}$$

Optics EXPRESS

the probability of observing parts n_1 and n_2 given the original Poisson-rate μ and the binomial success probability p follows as:

$$\begin{aligned} P(n_1, n_2|\mu, p) &= P_{\text{binomial}}(n_1, n_2|n_1+n_2, p)\, P_{\text{Poisson}}(n_1+n_2|\mu) \\ &= \frac{(n_1+n_2)!}{n_1!n_2!} p^{n_1}(1-p)^{n_2} \frac{e^{-\mu}\mu^{n_1+n_2}}{(n_1+n_2)!} \\ &= \frac{e^{-p\mu}(p\mu)^{n_1}}{n_1!} \frac{e^{-(1-p)\mu}((1-p)\mu)^{n_2}}{n_2!} \\ &= P_{\text{Poisson}}(n_1|p\mu)\, P_{\text{Poisson}}(n_2|(1-p)\mu). \end{aligned} \tag{3}$$

This proves that the split variables n_1 and n_2 independently satisfy Poisson statistics with rates $p\mu$ and $(1-p)\mu$.

Taking $p = 0.5$ and applying the random binomial splitting procedure per pixel we can split an entire image $E = \{n_k\}$, with n_k the observed photon count of pixel $k = 1, \ldots K$, with K the total number of pixels. The two resulting noise independent images are $E_1 = \left\{n_k^{(1)}\right\}$ and $E_2 = \left\{n_k^{(2)}\right\}$. Applying the Fourier Transform (FT) to the two images E_1 and E_2 gives $\hat{E}_1$ and $\hat{E}_2$. These can be used to compute the FRC [5] for a single image E by splitting it into E_1 and E_2 by the above procedure. We term this "1FRC":

$$1FRC = \frac{\left\langle \text{Re}\left\{\hat{E}_1 \cdot \hat{E}_2^*\right\}\right\rangle}{\sqrt{\left\langle \left|\hat{E}_1\right|^2\right\rangle \left\langle \left|\hat{E}_2\right|^2\right\rangle}}, \tag{4}$$

where the brackets indicate the averaging over rings in Fourier space. The image resolution can subsequently be assessed by thresholding the 1FRC curve at the value 1/7. Note that this image resolution value pertains to the image resolution of the input image E, not to the image resolution of the two image halves E_1 and E_2. Repeating the random binomial data splitting procedure (with $p = 0.5$) several times gives each time different images E_1 and E_2 with a different resolution and therefore we can use this to quantify the uncertainty in the 1FRC curve and the image resolution.

2.2. Spectral signal-to-noise-ratio

The two FTs of the split images can also be used to find the Spectral Signal-to-Noise-Ratio (SSNR) [7]. The FTs have a mean:

$$\hat{M} = \frac{\hat{E}_1 + \hat{E}_2}{2}, \tag{5}$$

and a variance:

$$\hat{V} = \left|\hat{E}_1 - \hat{M}\right|^2 + \left|\hat{E}_2 - \hat{M}\right|^2 = \frac{1}{2}\left|\hat{E}_1 - \hat{E}_2\right|^2. \tag{6}$$

The spectral noise variance in the original image $\hat{E} = \hat{E}_1 + \hat{E}_2$ follows:

$$\hat{N} = 2\hat{V} = \left|\hat{E}_1 - \hat{E}_2\right|^2. \tag{7}$$

The spectral signal power of the original image is then given by:

$$\hat{S} = \left|\hat{E}\right|^2 - \hat{N} = \left|\hat{E}_1 + \hat{E}_2\right|^2 - \left|\hat{E}_1 - \hat{E}_2\right|^2, \tag{8}$$

and the SSNR as:

$$SSNR = \frac{\hat{S}}{\hat{N}} = \frac{\left|\hat{E}_1 + \hat{E}_2\right|^2}{\left|\hat{E}_1 - \hat{E}_2\right|^2} - 1 = \frac{4\text{Re}\left\{\hat{E}_1 \cdot \hat{E}_2^*\right\}}{\left|\hat{E}_1 - \hat{E}_2\right|^2}. \tag{9}$$

Optics EXPRESS

By averaging over rings in Fourier space the 1FRC may be related to the SSNR by [7]:

$$1FRC \approx \frac{\langle SSNR \rangle}{1 + \langle SSNR \rangle}. \tag{10}$$

This relation may be used to relate the 1FRC curve to an overall assessment of noise and signal-to-noise ratio from a single image.

2.3. Raikov test

A theorem related to the above proof is Raikov's theorem [16], which states that if the sum of two independent random variables is Poisson distributed, then each of the two random variables is too. In fact, this theorem can be used to assess if all the pixels in an image follow Poissonian statistics, by analyzing the sum signal over all pixels. An experimental Cumulative Distribution Function (CDF) of the total signal can be measured by repeated imaging, and comparison to the Poissonian CDF by, e.g., a Kolmogorov-Smirnov (KS) test enables an assessment of the Poissonian nature of the imaging process.

2.4. Influence of readout noise and incorrect gain offset estimation

Implicitly we assumed that no other noise sources than Poisson noise are present in our input image. This is required in order to faithfully split an image into two while preserving the Poisson statistics in both splits. In case the gain or offset is incorrectly estimated and corrected for or in case there is significant (Gaussian) readout noise present this assumption is violated. In such cases it cannot be expected a priori that the two split image are uncorrelated (at high spatial frequencies). It turns out that the 1FRC converges to a non-zero plateau for high spatial frequencies.

We investigate the tolerances for such errors in Poisson statistics analytically here by writing the incorrectly observed photon count n_k of pixel k as a function of the expected photon count μ_k:

$$n_k = g'\mu_k + O' + g's_k, \tag{11}$$

where $g' = g/g_{\text{est}}$ is the ratio of the true gain g and the estimated gain $g_{\text{est}} = g + \Delta g$:

$$g' = \frac{g}{g_{\text{est}}} = \frac{1}{1 + \Delta g/g}, \tag{12}$$

where O' is the difference between the true offset O and the estimated offset $O_{\text{est}} = O + \Delta O$:

$$O' = \frac{O - O_{\text{est}}}{g_{\text{est}}} = -\frac{\Delta O}{g_{\text{est}}}, \tag{13}$$

and where s_k is the noise. For correctly estimated gain and offset we have $n_k = \mu_k$. Now we can Fourier transform Eq. (11) to find

$$\hat{n}_k = g'\hat{\mu}_k + KO'\delta_{k0} + g'\hat{s}_k, \tag{14}$$

where δ_{k0} denotes the delta peak at zero spatial frequency and K was the total number of pixels. The expected photon count satisfies $\hat{\mu}_k = \hat{H}_k\hat{x}_k$ with $\hat{H}_k$ the Optical Transfer Function (OTF) and x_k the fluorescent object. For large spatial frequencies, beyond the cutoff spatial frequency, we thus have $\hat{n}_k = g'\hat{s}_k$. According to mixed Poisson-Gauss statistics the noise correlation between pixels j and k is:

$$\langle s_j s_k \rangle_S = \left(\mu_k + \sigma^2\right)\delta_{jk}, \tag{15}$$

with σ the root mean square readout noise, and where the subscript 'S' indicates the expectation value for the the physically measured image signal.

Optics EXPRESS

The random binomial splitting gives pixel photon counts $n_k^{(1)}$ and $n_k^{(2)} = n_k - n_k^{(1)}$, where $n_k^{(1)}$ follows from the binomial distribution for n_k tries with success rate $p = 1/2$. At this point it is convenient to introduce a new random variable w_k defined via:

$$w_k = n_k^{(1)} - \frac{1}{2}n_k = \frac{1}{2}n_k - n_k^{(2)}. \tag{16}$$

Now the expectation values over the binomial distribution are:

$$\langle w_k \rangle_B = 0, \tag{17}$$

$$\langle w_j w_k \rangle_B = \frac{1}{4}n_k \delta_{jk}, \tag{18}$$

where the subscript 'B' indicates the expectation value over the random binomial split.

Taking the FT of the random variable w_k gives $\hat{w}_k$, with expectation value:

$$\langle |\hat{w}_j|^2 \rangle_B = \frac{1}{4}K\hat{n}_0, \tag{19}$$

with $\hat{n}_0$ the average estimated photon count per pixel. Taking a further expectation value over the measured image signal results in:

$$\langle \langle |\hat{w}_j|^2 \rangle_B \rangle_S = \frac{1}{4}\langle \hat{n}_0 \rangle_S = \frac{1}{4}K\left(g'\hat{\mu}_0 + O'\right), \tag{20}$$

with $\hat{\mu}_0$ the average expected photon count per pixel. For the FT of the noise we similarly find that:

$$\langle |\hat{s}_j|^2 \rangle_S = K\left(\hat{\mu}_0 + \sigma^2\right). \tag{21}$$

Now we have everything in place to compute the 1FRC plateau for high spatial frequencies, beyond the cutoff spatial frequency.

The nominator of the 1FRC depends on:

$$Re\left\{\hat{n}_k^{(1)}\hat{n}_k^{(2)*}\right\} = \frac{1}{4}|\hat{n}_k|^2 - |\hat{w}_k|^2. \tag{22}$$

Taking the expectation value over the binomial data splitting procedure gives:

$$\langle Re\left\{\hat{n}_k^{(1)}\hat{n}_k^{(2)*}\right\} \rangle_B = \frac{1}{4}\left(|\hat{n}_k|^2 - K\hat{n}_0\right). \tag{23}$$

Taking a further expectation value over the mixed Poisson-Gauss distribution of the measured image signal gives:

$$\begin{aligned}
\langle \langle Re\left\{\hat{n}_k^{(1)}\hat{n}_k^{(2)*}\right\} \rangle_B \rangle_S &= \frac{1}{4}\left(\langle |\hat{n}_k|^2 \rangle_S - K\langle \hat{n}_0 \rangle_S\right) \\
&= \frac{1}{4}\left(|g'\mu_k + KO'\delta_{k0}|^2 + g'^2\langle |s_k|^2 \rangle_S - K\langle \hat{n}_0 \rangle_S\right) \\
&= \frac{1}{4}\left(|g'\hat{\mu}_k + KO'\delta_{k0}|^2 + g'^2K\left(\hat{\mu}_0 + \sigma^2\right) - g'K\hat{\mu}_0 - KO'\right).
\end{aligned} \tag{24}$$

For high spatial frequencies, beyond the cutoff spatial frequency, we then find:

$$\langle \langle Re\left\{\hat{n}_k^{(1)}\hat{n}_k^{(2)*}\right\} \rangle_B \rangle_S \to \frac{1}{4}K\left(g'\left(g'-1\right)\hat{\mu}_0 - O' + g'^2\sigma^2\right). \tag{25}$$

Optics EXPRESS

A similar derivation for the terms in the denominator of the 1FRC results in an expectation value over the binomial distribution of the data split:

$$\langle Re\left\{\left|\hat{n}_k^{(1)}\right|^2\right\}\rangle_B = \langle Re\left\{\left|\hat{n}_k^{(2)}\right|^2\right\}\rangle_B = \frac{1}{4}\left(|\hat{n}_k|^2 + K\hat{n}_0\right). \tag{26}$$

The subsequent expectation value over the mixed Poisson-Gauss distribution of the measured image signal gives:

$$\langle\langle Re\left\{\left|\hat{n}_k^{(1)}\right|^2\right\}\rangle_B\rangle_S = \frac{1}{4}\left(|g'\hat{\mu}_k + KO'\delta_{k0}|^2 + g'^2K\left(\hat{\mu}_0 + \sigma^2\right) + g'K\hat{\mu}_0 + KO'\right).$$

For high spatial frequencies, beyond the cutoff spatial frequency, we find:

$$\langle\langle Re\left\{\left|\hat{n}_k^{(1)}\right|^2\right\}\rangle_B\rangle_S \to \frac{1}{4}K\left(g'\left(g'+1\right)\hat{\mu}_0 + O' + g'^2\sigma^2\right). \tag{27}$$

The plateau for the 1FRC at these high spatial frequencies thus becomes:

$$1FRC \to \frac{g'\left(g'-1\right) - O'/\hat{\mu}_0 + g'^2\sigma^2/\hat{\mu}_0}{g'\left(g'+1\right) + O'/\hat{\mu}_0 + g'^2\sigma^2\hat{\mu}_0}, \tag{28}$$

which is non-zero for non-zero readout noise, even in the case of correctly estimated gain ($g' = 1$) and offset ($O' = 0$), and therefore leads to errors in the estimation of the 1FRC resolution. This equation makes it possible to make a quantitative assessment of tolerances for such deviations of pure Poisson statistics in the imaging data.

The case of non-zero readout noise is of limited practical relevance, as for modern sCMOS camera's the readout noise is on the level of about one rms electrons, while typical average detected number of photons per pixel is at least one order higher even in background regions and much higher in foreground regions even for low light single molecule fluorescence imaging. Actually there is a simple mitigation to deal with non-zero readout noise. The mixed Poisson-Gauss distribution with expectation value μ and rms Gaussian noise σ is approximately Poissonian with expectation value $\mu + \sigma^2$. A mitigation procedure can be to add σ_{est}^2 to the estimated photon counts n_k, where σ_{est} is the estimated rms readout noise. If we then subsequently make the random binomial data split for each pixel, and subtract $\sigma_{\text{est}}^2/2$ from all pixels of the two split images, we find that the random variable w_k satisfies:

$$\langle\left|\hat{w}_j\right|^2\rangle_B = \frac{1}{4}K\left(\hat{n}_0 + \sigma_{\text{est}}^2\right). \tag{29}$$

The goal of this increase in the variance of the random binomial split is to cancel the rms readout noise term in the nominator of the 1FRC. The high spatial frequency plateau then becomes:

$$1FRC \to \frac{g'\left(g'-1\right) - O'/\hat{\mu}_0 + \left(g'^2\sigma^2 - \sigma_{\text{est}}^2\right)/\hat{\mu}_0}{g'\left(g'+1\right) + O'/\hat{\mu}_0 + \left(g'^2\sigma^2 + \sigma_{\text{est}}^2\right)\hat{\mu}_0}, \tag{30}$$

and now the readout noise term no longer leads to a non-zero value of the plateau in case of correct estimation of gain, offset, and rms readout noise ($g' = 1, O' = 0, \sigma_{\text{est}} = \sigma$).

Taking only an error in the estimation of the gain into account we find a high spatial frequency plateau:

$$1FRC \to \frac{g'-1}{g'+1} = \frac{\Delta g/g}{2 + \Delta g/g}, \tag{31}$$

As the 1FRC resolution is determined from the intersection with the threshold level $1/7 = 0.143$ relative gain errors $\Delta g/g$ of more than a few percent could already have an impact on the estimated

Optics EXPRESS

1FRC resolution. Gain estimation, even from a single exposure, luckily can be done to about 1-2% accuracy [17] and even better from many exposures [18].

If we look at the case with only an error in the estimation of the offset we find a high spatial frequency plateau:

$$1FRC \rightarrow \frac{-O'/\hat{\mu}_0}{2 + O'/\hat{\mu}_0} = \frac{\Delta O/(g\hat{\mu}_0)}{2 - \Delta O/(g\hat{\mu}_0)}\,. \tag{32}$$

We can conclude similarly as to the gain, that the offset error should only be a few percent of the average detected number of photons per pixel. For very sparse images this sensitivity may become prohibitive for application of the 1FRC concept. For typical to dense images the error in the estimation should be irrelevant [17].

3. Numerical simulations

We have tested the single image FRC concept in simulation. We have used a Matlab library image ('strawberries') as example object. Next, we applied low-pass filtering with the incoherent Optical Transfer Function with cutoff at 0.9× the maximum spatial frequency given by the image, i.e. this corresponds to slightly oversampling with pixelsize equal to $0.9 \times \lambda/(2\mathrm{NA})$, with λ the wavelength and NA the Numerical Aperture. The resulting image is normalized to one and subsequently multiplied with the average expected number of photons per pixel $\hat{\mu}_0$. In a next step noise is added first according to Poisson statistics, and then additional noise is added according to Gaussian statistics with rms value σ. The outcome is multiplied with a gain $g = 2$ and an offset $O = 100$ is added. These values are chosen as they are common values for current sCMOS cameras. This process of adding noise is repeated $M = 10$ times, giving M independent noisy simulated images. These simulated images are back converted to photon counts with different values for the estimated gain g_{est} and offset O_{est} as input for FRC computation. Standard double image FRC curves and resolution values are computed using image j and $j + 1$ as input, for $j = 1, \ldots M$, and where we identify image $j = M + 1$ with image 1. Single image FRC curves of equal average SNR values are found by first adding image j and $j + 1$, and then splitting the image

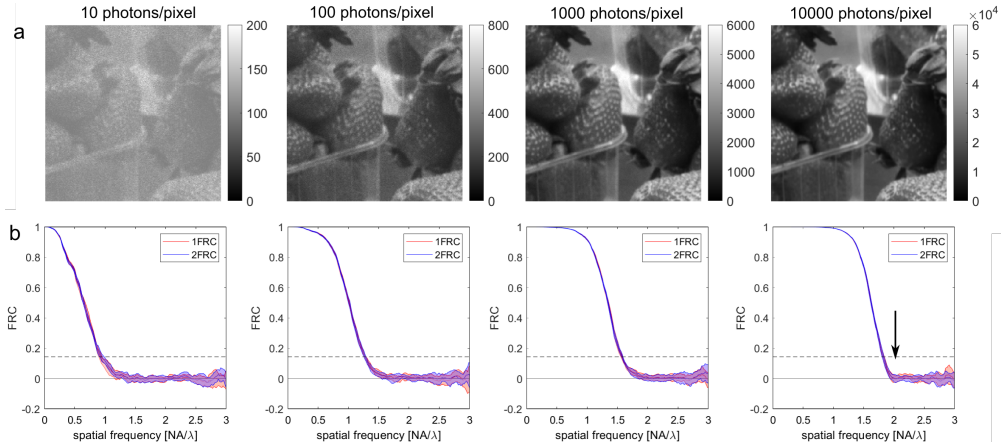

Fig. 1. Simulation of single and double image FRC resolution. (a) Examples of simulated widefield images for different values of the expected average number of photons per pixel. The gray scale bar indicates photon number. (b) Corresponding single ("1FRC") and double ("2FRC") image FRC curves. Both the mean FRC curves and the spread quantified by the standard deviation over the $M = 10$ curves are plotted. The FRC resolution approaches the diffraction limit at $2\mathrm{NA}/\lambda$ (black arrow in right graph of panel b) as the signal strength grows large.

Optics EXPRESS

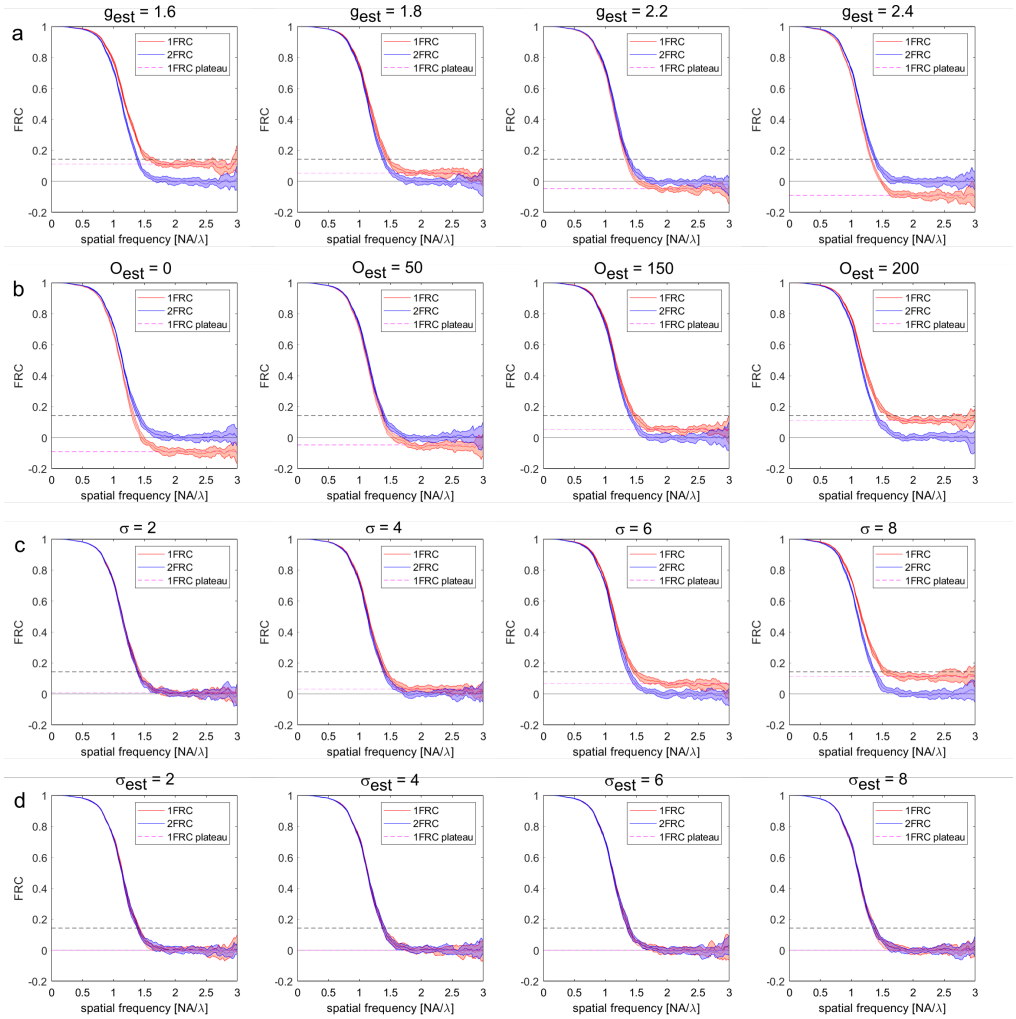

Fig. 2. Simulation of robustness single image FRC resolution. (a) Single and double image FRC curves for different values of the estimated gain, with $g = 2$ as simulation ground truth. (b) Single and double image FRC curves for different values of the estimated offset, with $O = 100$ as simulation ground truth. (c) Single and double image FRC curves for different values of the rms readout noise. (d) Single and double image FRC curves for different values of the rms readout noise with proposed compensation scheme. Both the mean FRC curves and the spread quantified by the standard deviation over the $M = 10$ curves are plotted. The magenta dashed lines indicate the predicted 1FRC plateau for the noise dominated high spatial frequencies according to Eq. (28).

into two independent noise halves according to the proposed procedure. The M FRC curves provide an indication of the statistical spread. For ensuring a fair comparison between 1FRC and 2FRC curves we keep the incident photon count for the one image for 1FRC equal to the two images for 2FRC. The threshold criterion of 1/7 takes into account the 50% SNR splitting [8].

Figure 1 shows the result of the simulation for different values of the average expected number of photons per pixel $\hat{\mu}_0$ and zero readout noise ($\sigma = 0$). Clearly, the 1FRC curves match very well with the 2FRC curves. We have also tested the sensitivity to errors in the gain and offset

Optics EXPRESS

estimation, and the effects of readout noise and of the proposed compensation for readout noise. Figure 2 shows the results of these simulations. In these simulations the average expected number of photons is taken to be $\hat{\mu}_0 = 250$, and the ground truth gain and offset are taken to be $g = 2$ and $O = 100$ to conform to typical settings in current sCMOS cameras. The predicted high spatial frequency 1FRC plateau Eq. (28) is in good agreement with the simulations for different settings for the estimated gain (compare Fig. 2(a)) and offset (compare Fig. 2(b)). The impact of large amounts of readout noise is also well described by Eq. (28), validating the dependence on the square of the rms readout noise (see Fig. 2(c)). The compensation strategy in the image splitting also works well, as can be seen in Fig. 2(d).

4. Experiment

4.1. Widefield microscopy

We have re-analyzed widefield microscopy datasets used in Ref. [5]. In short, images were taken from 11 different ROIs of a 200 nm bead sample with a fluorescence emission wavelength of 612 nm. The images were acquired with an IX71 Olympus inverted microscope with a 0.25/10× objective and with a 0.70/60× objective, and captured by a Hamamatsu ORCA-ER CCD camera with pixel size 6.45 μm. Each ROI was imaged $M = 20$ times, and a set of dark images was taken to subtract the offset. A gain calibration method was used to convert the pixel values to photon count [17]. Reference FRC resolutions were computed from FRC curves between subsequent images in the series of M images. Single image FRC resolutions were found by first adding subsequent images in the series, and then splitting the image in two noise independent halves following the proposed method. Figure 3 shows the resulting FRC resolutions, indicating a good correspondence between single and double image FRC resolutions. The readout noise compensation approach described in the Theory section was followed in view of the high readout noise level (8 photo-electrons/pixel rms). If the compensation step in the image splitting procedure is not followed, the 1FRC resolution values are underestimated depending on signal level. For high signal level the underestimation can be a few 10s of nm, for low signal level up to 100s of nm, in some cases the 1FRC resolution cannot be estimated at all if the plateau offset is higher than the 1/7 threshold. Visualization 1 and Fig. 3 show sample images and the full single and double FRC curves. It turns out that having a plateau near zero in the single image FRC curves at high spatial frequencies is sensitive to the gain setting within a few percent as expected from the Theory section.

The single image FRC curves appear to be slightly decreasing with spatial frequency in the noise dominated high spatial frequency region (compare Fig. 3(b))). The variance in Fourier space across the $M = 20$ noise independent acquisitions shows a similar small decrease with spatial frequency as well in the noise region. This indicates a small deviation from perfect Poisson statistics, and is consistent with an image blur at the camera level. We hypothesize that this effect is due to a camera imperfection such as crosstalk between neighbouring camera pixels. This would slightly smear out the signal as well as the noise pattern, resulting in a decreasing variance with spatial frequency in the noise region of Fourier space. We checked in simulation that blurring the noisy image with a Gaussian filter with a sigma smaller than half a pixel indeed gives rise to the same behaviour. In a next step we checked whether cameras of a more modern make than the ORCA-ER also show such behaviour. We imaged two color channels of a test slide (ThermoFisher FluoCells #1, Bovine Pulmonary Arterial Endothelial cells with mitochondria labeled with MitoTracker red, emission wavelength 599 nm, and actin labeled with Alexa Fluor 488 Phalloidin, emission wavelength 512 nm) with a Nikon Ti-E microscope body with a 100×/NA1.50 objective lens, equipped with an sCMOS camera (Teledyne Kinetix, 3200×3200 pixels, pixel size 6.45 μm, below 1e median readout noise). The estimated gain and offset were $g = 3.0$ and $O = 100$, respectively, $M = 10$ noise independent acquisitions were made. Figure 4 shows the result. The negative slope of the single image FRC plateau is strongly

Optics EXPRESS

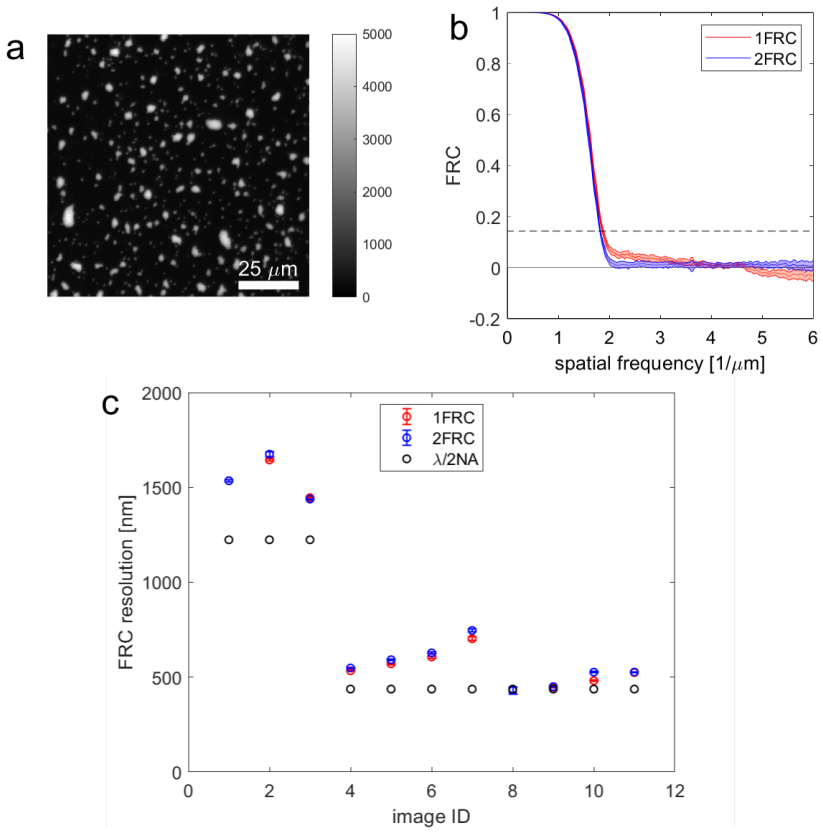

Fig. 3. Single image FRC resolution in widefield microscopy. (a) Example of widefield images (image ID 4). (b) Single and double image FRC curve pertaining to this image. (c) Single image ("1FRC") and double image ("2FRC") FRC resolution values, for 11 different ROIs and two different magnification/NA values of the objectives.

reduced, and single image FRC resolution values (291.6±1.1 nm and 302.1±1.4 nm for the actin and mitochondria channels, respectively) are close to the double image FRC resolution values (299.5±1.4 nm and 309.0±1.0 nm for the actin and mitochondria channels, respectively).

4.2. STED microscopy

We have applied the single image FRC concept to STimulated Emission Depletion (STED) [19] data of cellular membranes in fixed HeLa cells, stained with Nile Red, an exchangeable fluorophore label that enables multiple acquisitions of the same structure with minimal photobleaching. The images were acquired with an inverted TCS SP8 3X STED microscope (Leica Microsystems, Mannheim, Germany) equipped with a 100x/1.4 NA oil immersion objective (Leica HC PL APO CS2 - STED White). Nile Red was excited with 561 nm laser light derived from a 80 MHz pulsed White Light Laser (Leica Microsystems, Mannheim Germany) and the stimulated emission was performed with a 80 MHz pulsed laser emitting at 775 nm (Leica Microsystems, Mannheim Germany). The scanning pixel size was set to 20 nm. All further details on sample preparation and imaging settings are reported in Ref. [20]

The sample was imaged for 3 different settings with 4 repeated, noise independent acquisitions. As a reference, a single image was captured at zero depletion laser power, i.e. this corresponds to a regular confocal image. Single and double image FRC curves and resolution values were

Optics EXPRESS

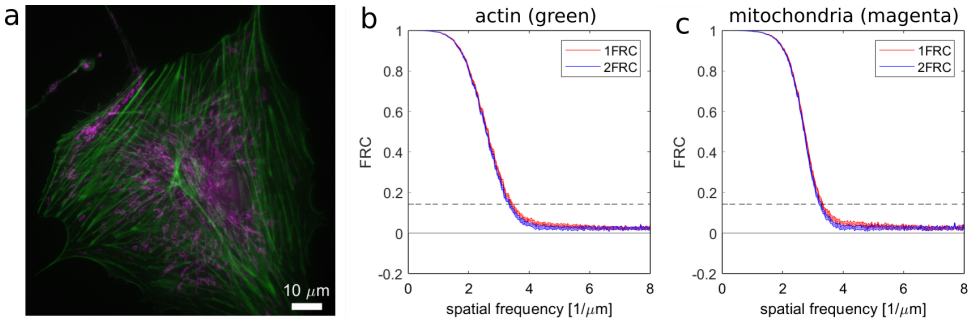

Fig. 4. Single image FRC resolution in widefield microscopy. (a) Cropped part of two-color widefield microscopy image of test slide. (b) Single ("1FRC") and double ("2FRC") image FRC curve pertaining to the actin (green) channel. (c) Single ("1FRC") and double ("2FRC") image FRC curve pertaining to the mitochondria (magenta) channel. Both the mean FRC curves and the spread quantified by the standard deviation over the $M = 10$ curves are plotted.

obtained from the 4 repeated acquisitions in the same way as for the widefield data, giving 4 FRC curves and FRC resolution values. For the reference confocal image, 5 randomly different image splits were processed for an assessment of the statistical spread of the single image FRC curve and resolution. Figure 5 shows the results of the analysis. It turns out that the agreement between single and double image FRC is very well, supporting the validity of the single image FRC concept. The FRC resolution improves with increasing depletion laser power, as expected, but part of the potential improvement of a smaller STED spot is canceled by a decrease in collected fluorescence signal. This results in an increase in noise level, as is apparent from the insets in Fig. 5(b)-(e). For comparison we have plotted the predicted STED resolution [21]:

$$R_{\mathrm{STED}} = \frac{\lambda}{2\mathrm{NA}\sqrt{1 + I_{\mathrm{dep}}/I_0}} \tag{33}$$

where we have set $I_0 = 7$ to make the curve fit through the first two data points, which have high SNR. The deviation of the FRC resolution from this ultimate limit increases with depletion laser power, because of the decrease in fluorescence signal. We also show the image resolution according to decorrelation analysis [22]. These resolution estimates are a bit higher than the FRC based estimates, but give the same trend as a function of depletion laser power.

4.3. *Rescan confocal microscopy and image scanning microscopy*

We analyzed images of a single sample of the so-called synaptonemal complex acquired with both with a Zeiss Airyscan setup, based on the Image Scanning Microscopy (ISM) super-resolution technique [13], and with a Rescan Confocal Microscopy (RCM, confocal.nl) setup [12] operating on a Nikon microscope body. The two microscopes had somewhat different imaging parameters, in particular the numerical aperture (NA = 1.40 for Zeiss and NA = 1.45 for Nikon) and the back projected pixel size ($a = 42.6$ nm for Zeiss and $a = 43.3$ nm for Nikon). The higher NA of the Nikon machine implies that more light is collected for the same exposure time and that the depth of focus is smaller. The emission wavelength of the used fluorophore was 520 nm. The same datasets were used in the study of the concept of an ideal OTF and application thereof in Wiener filtering [23]. A detailed description of the data processing steps to construct the confocal and ISM images from the separate Airyscan detector segments can be found there.

The gain and offset corrected data are split into two noise-independent halves with the random binomial splitting procedure and the single image FRC curves are subsequently computed, giving

Optics EXPRESS

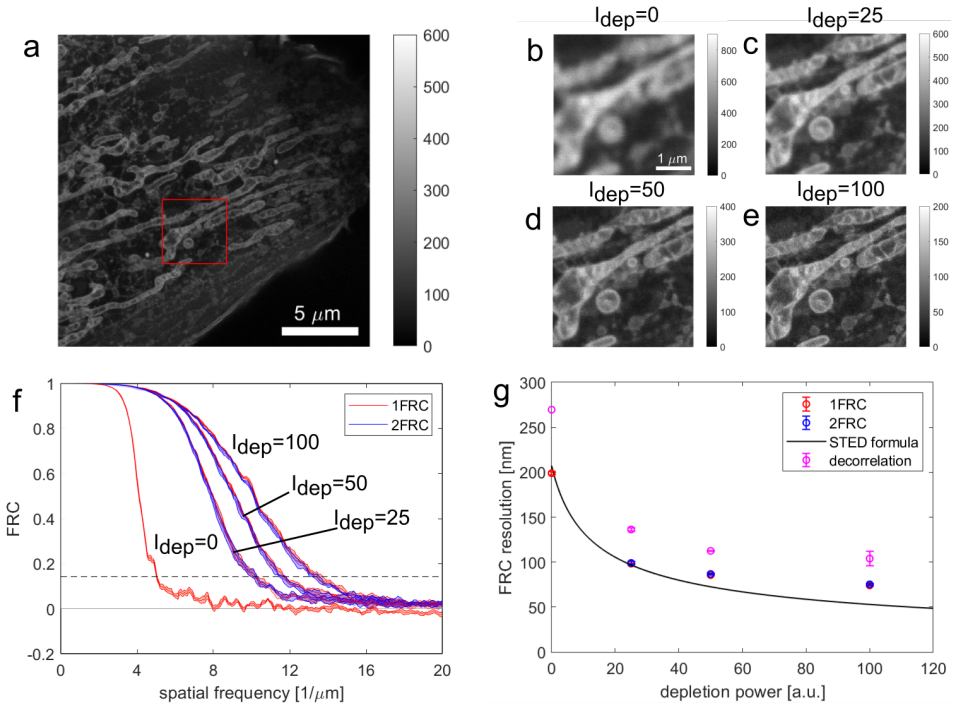

Fig. 5. Single image FRC on STED data. (a) STED image of HeLa cells labelled with Nile Red, sowing the mitochondrial ultrastructure. (b)-(e) Insets (red square in (a)) at different depletion laser powers. (f) Single and double image FRC curves for different depletion laser powers. Both the mean FRC curves and the spread quantified by the standard deviation over the $M = 4$ curves are plotted. (g) Single and double image FRC resolution as a function of laser power, in comparison to STED resolution formula Eq. (33), and decorrelation analysis [22].

finally rise to a set of 1FRC resolution values. The 1FRC curves for the confocal/ISM dataset have a plateau at high spatial frequencies that is very nearly zero (median value -0.004 above widefield/confocal diffraction limit), whereas the 1FRC curves for the RCM dataset have a plateau at high spatial frequencies that is slightly positive (median value 0.06 above widefield/confocal diffraction limit), possibly due to effects of fixed pattern noise, giving a positive correlation offset after the image splitting approach. This has the consequence that the 1FRC resolution for RCM is slightly underestimated.

Figure 6 shows the results of this analysis. The 1FRC resolution for the confocal case in focus is 191 nm, almost equal to the diffraction limit ($\lambda/2\mathrm{NA}$ = 186 nm with NA = 1.40), and getting worse out of focus. We find comparable 1FRC values of around 159 nm for ISM in focus and 165 nm for RCM in focus (with diffraction limit of 179 nm), 20% and 16% better than the confocal case, respectively. This improvement factors are less than the expected factor of around $\sqrt{2}$ but match with qualitative impressions of the images. The 1FRC resolution for the RCM case increases steeper away from focus, which can be related to the higher NA and the resulting lower depth of focus of the Nikon setup compared to the Zeiss setup. This can account for a 13% difference, based on the scaling of the depth of focus proportional to $\lambda/(1-\cos\alpha)$ with $\sin\alpha = \mathrm{NA}/n$, assuming a sample refractive index $n = 1.515$.

Optics EXPRESS

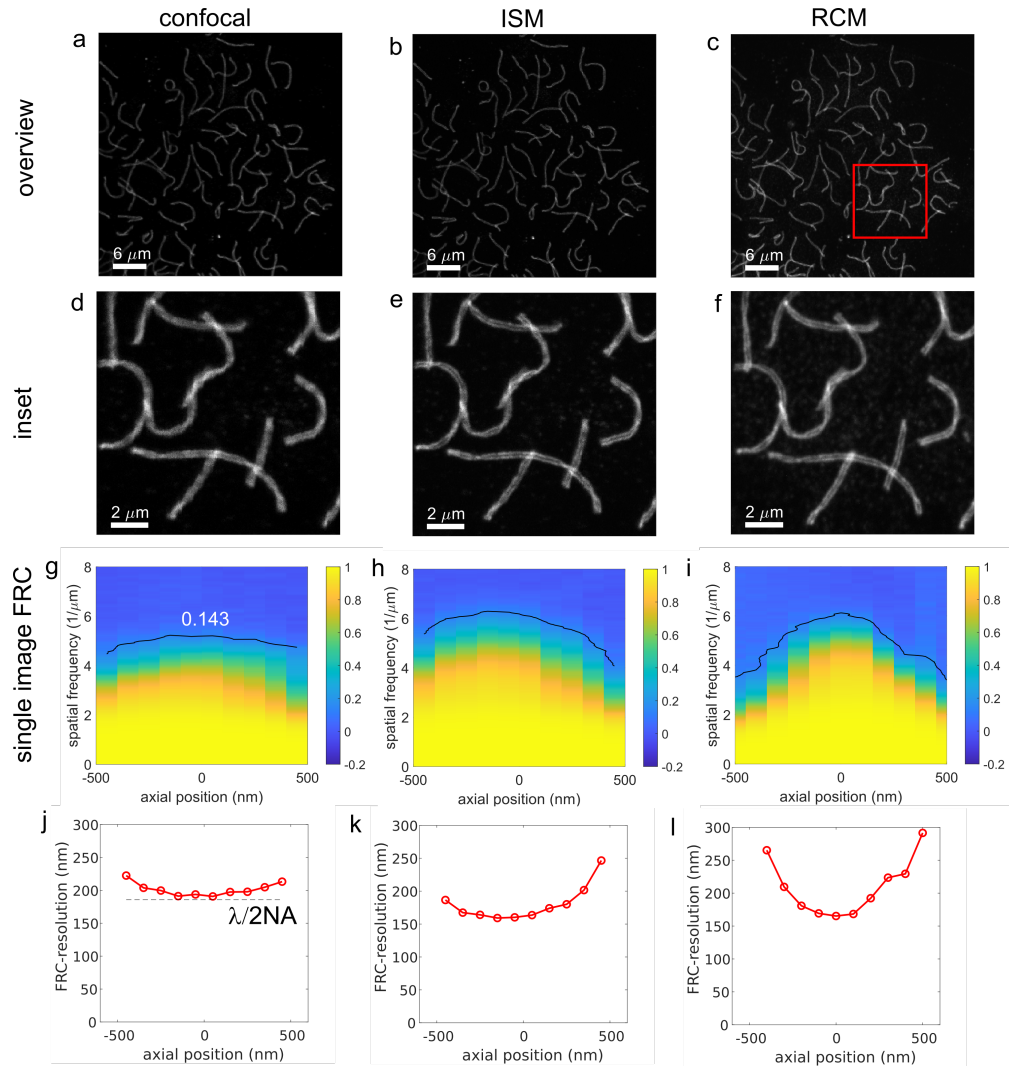

Fig. 6. Single image FRC for confocal, ISM and RCM techniques. (a)-(c) Images of synaptonemal complex with conventional confocal, ISM and RCM. (d)-(f) Insets showing the similarly improved resolution of ISM and RCM compared to confocal. (g)-(i) Quantization of resolution by single image FRC for a through-focus stack for confocal, ISM, and RCM. (j)-(l) Single image FRC resolution values as a function of focus position for confocal (NA = 1.0), ISM, and RCM.

4.4. *Transmission electron microscopy*

We have also tested the single image FRC concept on cryogenic Transmission Electron Microscopy (cryo-TEM) image data. Data of mouse H-chain apoferritin were acquired with a JEM3200-FSC microscope operated at 300 kV in zero-loss imaging mode using a 20 eV slit centered at 0 eV. Movies were recorded over 50 frames accumulating to a total exposure of 46 e^-/ Å^2 with a Gatan K2 Summit detector at 0.495 Å pixel size. Cryo-TEM data stands out because of its extremely low signal levels. The average number of detected electrons across the frames was just 0.435 e^-/pixel. The fifty frames were processed to compute $M = 25$ single and double image FRC

Optics EXPRESS

curves by pairing even and odd frames, following practice in the TEM field. Figure 7 shows the comparison of the resulting single and double image FRC resolution, indicating a very good match between the two, also at extremely low signal level.

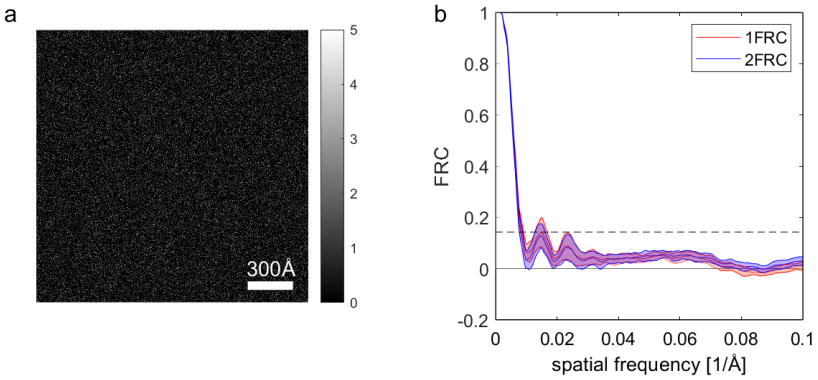

Fig. 7. Single and double image FRC for TEM. (a) Example image indicating the very low signal values of TEM data. (b) Corresponding single ("1FRC") and double ("2FRC") image FRC curves. Both the mean FRC curves and the spread quantified by the standard deviation over the $M = 25$ curves are plotted. The FRC resolution values were a comparable 42.4±2.1 Å (1FRC) and 43.6±2.3 Å (2FRC).

5. Conclusion

In summary, we have demonstrated FRC resolution derived from single images, making use of the properties of Poisson statistics that dominate the noise behaviour. The key advantage is that it removes the necessity to acquire pairs of images for the mere sake of image resolution assessment, and overcomes drawbacks in sampling of a checkerboard based image splitting. We have shown the validity and usefulness of single image FRC on different fluorescence microscopy modalities, both scanning based and camera based, employing different photo-detectors and camera's.

It turned out that current methods to estimate gain and offset are accurate and precise enough to make our single image FRC approach work. The sensitivity of the image splitting procedure to deviations from Poisson statistics offers an opportunity to eliminate the prior estimation of gain and offset from the overall analysis. When it can be firmly established a priori that imaging follows shot noise behaviour, then keeping the single image FRC plateau at high spatial frequencies near zero is a means to estimate gain and/or offset. Similarly, a non-zero slope of the single image FRC plateau can be used to detect blurring or sharpening of the underlying image with noise governed by Poisson statistics.

The single image FRC can be applied to settings where the sample or scene is not static, e.g. a time-series of a moving object, or when the structure of the sample is changing as in cryo-EM during radiation exposure over time frames.

In addition to its use as a resolution metric, single image FRC can also be used in filtering approaches and as a stopping criterion in deconvolution approaches, as outlined in Ref. [11]. The image splitting that underlies the single image FRC can also be used to establish two noise independent inputs for a deconvolution algorithm [24]. Comparison of the two deconvolution outputs by FRC can subsequently be used as stopping criterion for intrinsically ill-convergent algorithms, optimizing the final image resolution that can be achieved with deconvolution. It is imperative to split the image data in the processing pipeline when Poisson statistics applies. This is at the raw data level, after gain and offset correction.

Optics EXPRESS

In a future step, we envision the application of the random binomial splitting procedure to methods where a higher-resolution image reconstruction is made from a set of raw images, as in Structured Illumination Microscopy (SIM) [10]. There, different rotations and translations of a spatially periodic illumination pattern result image acquisitions E_{rn} where $r = 1, 2, \ldots, M_r$ labels the rotations and $n = 1, 2, \ldots, M_t$ labels the translations. Typically $M_r = 3$ or $M_r = 5$ rotations and $M_t = 3$ (for 2D-SIM) or $M_t = 5$ (for 3D-SIM) translations are used. Now the random binomial data splitting procedure can be applied to all $M_r \times M_t$ raw images separately. All the resulting split images can then be used as input for generating two noise independent SIM reconstructions E_1^{SIM} and E_2^{SIM}. These in turn can be used to calculate the FRC curve without having to repeat the SIM acquisition. The image data must be split at the input level, just as for the case of deconvolution. Splitting the outcome of an image reconstruction for computation of an FRC curve is incorrect. In this case the reconstruction process will introduce correlations and bias to the resolution estimate. This procedure is in accordance with best practice in single particle analysis in cryo-electron microscopy [25].

Funding. European Research Council (101055013); Nederlandse Organisatie voor Wetenschappelijk Onderzoek (17046).

Acknowledgments. We are grateful to Marko Lampe (EMBL Heidelberg) and Mike Heilemann (Goethe-University Frankfurt) for providing experimental STED data, and to Christoph Spahn (MPI Marburg) for technical advice. We thank the Advanced Light Microscopy Facility (ALMF) at the European Molecular Biology Laboratory (EMBL) and Leica Microsystems for access to the STED microscope and support. We are grateful to Jeroen Kole (confocal.nl) for making ISM and RCM data available and to Arjen Jakobi (TU Delft) for providing experimental TEM data. We thank Yuchen Deng, Erik Franken and Remco Schoenmakers (ThermoFisher, Eindhoven) for inspiring discussions on the topic.

Disclosures. The authors declare no conflicts of interest.

Data availability. Raw image data is available at [26], Matlab code is available at [27].

References

1. T. A. Klar, S. Jakobs, M. Dyba, *et al.*, "Fluorescence microscopy with diffraction resolution barrier broken by stimulated emission," Proc. Natl. Acad. Sci. U. S. A. **97**(15), 8206–8210 (2000).
2. E. Betzig, George H Patterson, Rachid Sougrat, *et al.*, "Imaging Intracellular Fluorescent Proteins at Nanometer Resolution," Science **313**(5793), 1642–1645 (2006).
3. M. J. Rust, M. Bates, and X. Zhuang, "Sub-diffraction-limit imaging by stochastic optical reconstruction microscopy (STORM)," Nat. Methods **3**(10), 793–796 (2006).
4. A. Sharonov and R. M. Hochstrasser, "Wide-field subdiffraction imaging by accumulated binding of diffusing probes," Proc. Natl. Acad. Sci. U. S. A. **103**(50), 18911–18916 (2006).
5. R. P. J. Nieuwenhuizen, K. A. Lidke, M. Bates, *et al.*, "Measuring Image Resolution in Optical Nanoscopy," Nat. Methods **10**(6), 557–562 (2013).
6. M. van Heel, "Similarity measures between images," Ultramicroscopy **21**(1), 95–100 (1987).
7. M. Unser, B. L. Trus, and A. C. Steven, "A new resolution criterion based on spectral signal-to-noise ratio," Ultramicroscopy **23**(1), 39–51 (1987).
8. P. B. Rosenthal and R. Henderson, "Optimal Determination of Particle Orientation, Absolute Hand, and Contrast Loss in Single-particle Electron Cryomicroscopy," J. Mol. Biol. **333**(4), 721–745 (2003).
9. G. Tortarolo, M. Castello, A. Diaspro, *et al.*, "Evaluating image resolution in STED microscopy," Optica **5**(1), 32–35 (2018).
10. R. Heintzmann and T. Huser, "Super-Resolution Structured Illumination Microscopy," Chem. Rev. **117**(23), 13890–13908 (2017).
11. S. Koho, G. Tortarolo, M. Castello, *et al.*, "Fourier ring correlation simplifies image restoration in fluorescence microscopy," Nat. Commun. **10**(1), 3103 (2019).
12. G. M. R. De Luca, R. M. P. Breedijk, R. A. J. Brandt, *et al.*, "Re-scan confocal microscopy: scanning twice for better resolution," Biomed. Opt. Express **4**(11), 2644–2656 (2013).
13. C. B. Müller and J. Enderlein, "Image Scanning Microscopy," Phys. Rev. Lett. **104**(19), 198101 (2010).
14. A. G. York, (@AndrewGYork) "Can you "coinflip split" the image? Meaning, scale image counts to photoelectrons, then flip a coin for each photoelectron to decide if it belongs in imaginary subexposure 1 or imaginary subexposure 2?" *X*, March 15, 2018, https://twitter.com/AndrewGYork/status/974311139956875265.
15. D. L. Fried, "Noise in Photoemission Current," Appl. Opt. **4**(1), 79–80 (1965).
16. D. Raikov, "On the decomposition of Poisson laws," Dokl. Acad. Sci. URSS **14**, 9–11 (1937).
17. R. Heintzmann, P. K. Relich, R. P. J. Nieuwenhuizen, *et al.*, "Calibrating photon counts from a single image," arXiv, arXiv:1611.05654 (2018).

Optics EXPRESS

18. R. Diekmann, J. Descamps, Y. Li, *et al.*, "Photon-free (s)CMOS camera characterization for artifact reduction in high- and super-resolution microscopy," Nat. Commun. **13**(1), 3362 (2022).
19. G. Vicidomini, P. Bianchini, and A. Diaspro, "STED super-resolved microscopy," Nat. Methods **15**(3), 173–182 (2018).
20. C. Spahn, J. B. Grimm, L. D. Lavis, *et al.*, "Whole-Cell, 3D, and Multicolor STED Imaging with Exchangeable Fluorophores," Nano Lett. **19**(1), 500–505 (2019).
21. V. Westphal and S. W. Hell, "Nanoscale Resolution in the Focal Plane of an Optical Microscope," Phys. Rev. Lett. **94**(14), 143903 (2005).
22. A. Descloux, K. S. Grußmayer, and A. Radenovic, "Parameter-free image resolution estimation based on decorrelation analysis," Nat. Methods **16**(9), 918–924 (2019).
23. S. Stallinga, N. Radmacher, A. Delon, *et al.*, "Optimal transfer functions for bandwidth-limited imaging," Phys. Rev. Res. **4**(2), 023003 (2022).
24. J. Becker, C. Russell, A. York, *et al.*, "Knowing when to stop: a data-driven termination criterion for iterative deconvolution," *Microscience Microscopy Congress* (2023).
25. R. Henderson, "Avoiding the pitfalls of single particle cryo-electron microscopy: Einstein from noise," Proc. Natl. Acad. Sci. U. S. A. **110**(45), 18037–18041 (2013).
26. B. Rieger and S. Stallinga, "Data underlying the publication: Single Image Fourier Ring Correlation," 4TU.ResearchData (2024), https://doi.org/10.4121/3f285c07-93c0-4a8a-bbcd-bc60ed749c88.v1.
27. B. Rieger and S. Stallinga, "1FRC," Delft University of Technology GitLab (2024), https://gitlab.tudelft.nl/imphys/ci/1frc.